



Size controllable synthesis of single-crystal ferroelectric $\text{Bi}_4\text{Ti}_3\text{O}_{12}$ nanosheet dominated with $\{001\}$ facets toward enhanced visible-light-driven photocatalytic activities

Hongquan He^{a,b}, Jiao Yin^a, Yingxuan Li^{a,*}, Ying Zhang^{a,b}, Hengshan Qiu^a, Jinbao Xu^a, Tao Xu^c, Chuanyi Wang^{a,*}

^a Laboratory of Environmental Sciences and Technology, Xinjiang Technical Institute of Physics and Chemistry; Key Laboratory of Functional Materials and Devices for Special Environments, Chinese Academy of Sciences, Urumqi, Xinjiang 830011, China

^b University of Chinese Academy of Sciences, Beijing 100049, China

^c Department of Chemistry and Biochemistry, Northern Illinois University, DeKalb, IL 60115, USA

ARTICLE INFO

Article history:

Received 14 January 2014

Received in revised form 25 February 2014

Accepted 2 March 2014

Available online 12 March 2014

Keywords:

Molten salt synthesis

$\text{Bi}_4\text{Ti}_3\text{O}_{12}$

Photocatalytic

Ferroelectric

Internal electric fields

ABSTRACT

Highly crystallized single crystal $\text{Bi}_4\text{Ti}_3\text{O}_{12}$ nanosheets with dominant $\{001\}$ facets were synthesized by heating a stoichiometric composition of $\alpha\text{-Bi}_2\text{O}_3$ and TiO_2 in molten NaCl-KCl at 800°C for 2 h. Effects of the amount of the added molten salts (their mole ratio (M) to nominal $\text{Bi}_4\text{Ti}_3\text{O}_{12}$ varied from 4 to 60 and the samples were denoted as BTO- M) on the size distribution and photoactivity of the resulting products were systematically evaluated. The side length of as-prepared $\text{Bi}_4\text{Ti}_3\text{O}_{12}$ gradually decreases by increasing the addition of molten salts, and the minimal side length is achieved in the sample BTO-50. As a result, the sample BTO-50 shows the best photocatalytic kinetics in photodegradation of rhodamine B (RhB) under visible-light irradiation, which is about 8.65 times faster than that of the sample BTO-0 obtained by a traditional solid-state reaction method, demonstrating the superiority of the present molten salts synthesis for bismuth titanate. The improved photocatalytic kinetics of BTO- M is a concert of several factors including the highly faceted surfaces, thin flakes that shorten the charge transport distance to the surface, as well as the internal electric fields produced by the spontaneous polarization in the BTO-50 sample that facilitate the separation of photoinduced charges as evidenced by Kelvin probe force microscopy. Electrochemical impedance spectroscopy further reveals that under visible-light, the electron transfer resistance of the BTO-50 decreases to nearly 50% of that of the BTO-0 sample.

© 2014 Elsevier B.V. All rights reserved.

1. Introduction

Recently, photocatalysis has received extensive attention due to its great potential in tackling energy and environmental challenges [1–3]. Among all photocatalysts, TiO_2 -based catalysts appear as the most promising candidates for their high photocatalytic activities, environmental benign nature and large abundance. Unfortunately, the large band gap ($\sim 3.2\text{ eV}$) of pristine TiO_2 makes it only photoactive in UV light, which limits its efficiency powered by sunlight, as UV light only accounts for 5% energy of the entire solar spectrum while 43% solar energy resides in visible region [4]. As such, it is highly desirable to develop visible-light-driven photocatalysts. To achieve this goal, a typical approach is to modify wide bandgap

active photocatalysts through substitutional doping, as demonstrated in LaTiO_2N [5], TaON [6], $\text{Sm}_2\text{Ti}_2\text{S}_2\text{O}_5$ [7], $\text{Sr}_2\text{Nb}_2\text{O}_{7-x}\text{N}_x$ [8], as well as $\text{TiO}_{2-x}\text{N}_x$ [9] for anion doping, and in $\text{InTaO}_4\text{:Ni}$ [10], $\text{TiO}_2\text{:Sb/Cr}$ or $\text{SrTiO}_3\text{:Sb/Cr}$ [11], and $\text{La}_2\text{Ti}_2\text{O}_7\text{:Cr/Fe}$ [12], for cation doping. However, it is usually difficult to achieve a high photocatalytic activity from a doped material because of the small amount of visible-light absorbed by a discrete doping level [13] and some of them behave as the trapping center for photoinduced charge carriers (e^-/h^+) [14]. Therefore, considering the stability of substituted anions under reaction conditions, the most reliable candidates for visible-light-driven photocatalysts would be single phase metal oxides [15].

As reported, the activities of the photocatalysts are especially dependent on the exposed facets of the particles [16–18]. For instance, the BiOCl single-crystalline nanosheets [19] with exposed $\{001\}$ facets exhibit higher activity than that of the $\{010\}$ faceted sample for direct semiconductor photo-assisted pollutant

* Corresponding authors. Tel.: +86 9913835879; fax: +86 9913838957.

E-mail addresses: yxli@ms.xjb.ac.cn (Y. Li), cywang@ms.xjb.ac.cn (C. Wang).

degradation under UV light. In the oxidation of toluene to benzaldehyde, anatase TiO_2 nanoparticles with dominant $\{001\}$ facets synthesized by Li et al. exhibit a factor of two times enhancement in photocatalytic activity over that of nanoparticles with predominant $\{101\}$ facets [20,21]. Thus, synthesis of nanoparticles with desired exposed facets could lead to major breakthrough in exploring the factors that can improve the kinetics of photocatalytic processes.

Bismuth titanate ($\text{Bi}_4\text{Ti}_3\text{O}_{12}$, BTO), consisting of pseudoperovskite ($\text{Bi}_2\text{Ti}_3\text{O}_{10}$)²⁻ units sandwiched in between the bismuth oxygen (Bi_2O_2)²⁺ layers along the *c* axis, has been widely explored for its applications in optical, ferroelectric, and optoelectronic devices [22–24]. In recent years, it has been found that BTO exhibits high photocatalytic activities under visible-light [25]. Therefore, several methods, such as chemical solution decomposition [26], hydrothermal synthesis [27,28], and electrospinning [29], have been developed to obtain BTO-based photocatalysts with different nanostructures. However, most of these reported routes involve the use of expensive precursors or complicated synthetic processes. In addition, limited work has been reported on the synthesis of BTO photocatalysts with controlled shapes and exposed facets.

Molten salt synthesis (MSS) method is based on utilizing a mixture of molten salts as a highly reactive medium [30]. In particular, it is one of the simplest, highly cost-effective approaches accessible for large-scale preparing crystalline, single-phase nanoscale materials. Utilizing eutectic salt compositions as a highly reactive medium commonly needs a relatively low reaction temperature, where the mobility of ions in these molten salts (10^{-5} – 10^{-8} cm^2/s) is approximately 10^{10} times higher than in the solid state ($\sim 10^{-18}$ cm^2/s) [31,32]. Thus, it often needs much shorter time to obtain high crystalline material than by solid state method. Owing to these advantages, this method has been used widely to prepare titanates [33], niobates [34,35], tantalates [36,37] and ferrites [38] using chlorides, sulfates or carbonates as salt medium. It is anticipated that the molten salt synthesis method can be extended to preparing many other kinds of materials.

In this work, a facile molten salt synthesis (MSS) methodology has been developed to achieve size-controlled BTO nanosheets with predominant exposure of $\{001\}$ facets by simply varying the mole ratio (*M*) of salts (NaCl and KCl) to $\text{Bi}_4\text{Ti}_3\text{O}_{12}$ from 4 to 60. Interestingly, the size of the BTO-*M* samples decreases with the increase of the *M* value, which enhances the BET surface area of the particles for improved the photocatalytic activities. Meanwhile, BTO single crystals exhibit spontaneous polarization (*P*_s) of $4 \mu\text{C cm}^{-2}$ along the *c*-axis [24,39]. Thus, the formed internal electric field along $[001]$ direction can promote the separation of photoinduced charges. This effect is proven by tracking the surface-potential change of the BTO-50 sample in dark and under visible-light irradiation using kelvin probe force microscopy (KPFM) analysis. It is the first time to investigate how the ferroelectric nature of BTO affects the photocatalytic activities. In addition, the nanosheet structure also shortens the separation distance of photoinduced electron–hole pairs along $[001]$ direction, as evidenced by the improved photocatalytic kinetics by a factor of about 8 times higher than that of BTO-0 sample prepared through a traditional solid-state reaction method.

2. Experimental details

2.1. The preparation of BTO-*M* samples and electrodes

$\text{Bi}_4\text{Ti}_3\text{O}_{12}$ was synthesized by a molten salt synthesis (MSS) method. $\alpha\text{-Bi}_2\text{O}_3$ (99.9%, Sinopharm Chemical Reagent Co., Ltd.) and Degussa (P25) TiO_2 were used as starting materials. A typical procedure for preparing $\text{Bi}_4\text{Ti}_3\text{O}_{12}$ powdery sample is described as following: first, powders of $\alpha\text{-Bi}_2\text{O}_3$ and P25 with appropriate stoichiometric amounts were mixed according to the composition

of $\text{Bi}_4\text{Ti}_3\text{O}_{12}$. Then, NaCl and KCl were taken as the cosolvents at a mole ratio of NaCl: KCl: $\text{Bi}_4\text{Ti}_3\text{O}_{12} = M:M:1$ (*M* = 4, 8, 16, 32, 40, 50, 60). The mixture was continuously grinded for over 30 minutes with an agate mortar and pestle. The resulting mixture was then heated at 800 °C for 2 hours in air. The mixed NaCl and KCl (mole ratio is 1:1) can be totally melted at 800 °C according to the eutectic point, which is the key for the preparation of $\text{Bi}_4\text{Ti}_3\text{O}_{12}$. The final products were gently washed with deionized water several times to wash off the cosolvents, followed by desiccation at 60 °C in air. The as-prepared products are denoted as BTO-4, BTO-8, BTO-16, BTO-32, BTO-40, BTO-50, BTO-60, respectively. For comparison, $\text{Bi}_4\text{Ti}_3\text{O}_{12}$ (denoted as BTO-0) was also prepared via a traditional solid-state reaction (SSR) under the same conditions, except that no NaCl or KCl was used as solvent.

For electrochemical characterization, the BTO-*M* electrodes were prepared as following: 6 mg of BTO-*M* samples were added to 600 μL solution containing 200 μL of absolute ethyl alcohol ($\text{CH}_3\text{CH}_2\text{OH}$) and 400 μL of Nafion DE 520 solution (5 wt% Nafion, 50 ± 3 wt% water, and 48 ± 3 wt% propanol, EW is 1000, DuPont). The mixture was then ultrasonically dispersed for 20 min. Finally, 100 μL of the well dispersive BTO-*M* slurry were cast onto cleaned ITO glass substrates ($<7 \text{ ohm/square}$) to form uniform film electrodes. The BTO-*M* electrodes were finally obtained after sintering at 100 °C for 2 h.

2.2. Characterization of samples

X-ray diffraction (XRD) patterns of the samples were collected on Bruker D8 powder diffractometer over scattering angles from 5° to 80° using $\text{Cu K}\alpha$ radiation. The morphologies and sizes of the samples were studied by scanning electron microscopy (SEM, ZEISS SUPRA55VP). Transmission electron microscopy (TEM) characterization was performed on a JEOL-JEM 2100 electron microscope. Optical properties of the obtained powders were studied via UV–vis absorption spectroscopy using a Shimadzu SolidSpec-3700DUV spectrophotometer. Specific surface areas of samples were measured by the BET method (N_2 adsorption) in a nitrogen adsorption apparatus (Quantachrome 1900 Corporate Drive).

Kelvin probe force microscopy (KPFM) measurement was carried out using an Asylum Research MFP-3DTM atomic force microscope in non-contact mode. The cantilever coated with a PtIr alloy was used for KPFM modes. The BTO-50 sample was tested both in dark environment and under visible-light irradiation. A 300 W Xe lamp with a 420 nm UV filter was used as the visible-light source.

Electrochemical impedance spectroscopy (EIS) measurement was conducted between 0.01 Hz and 100 kHz frequency using a potential of 0.17 V with the CHI660E instrument. A three-electrode system was used, in which a BTO-*M*/ITO electrode (4 cm^2), a saturated calomel electrode (SCE), and a platinum sheet (4 cm^2) were employed as the working electrode, the reference electrode and the auxiliary electrode, respectively. The 0.1 M KCl and 0.1 M $\text{K}_3[\text{Fe}(\text{CN})_6]/\text{K}_4[\text{Fe}(\text{CN})_6]$ (1:1) were used as the detecting electrolyte. A 300 W Xe lamp held at 10 cm from the quartz cell with a 420 nm UV filter was used as the visible-light source.

2.3. Photocatalytic measurements

The photocatalytic activities of the as-prepared products were measured by examining the photodegradation of organic dye RhB under visible-light irradiation ($\lambda > 420 \text{ nm}$) at ambient temperature. A 300 W Xe lamp held at 10 cm from the sample with a 420 nm UV filter was used as the visible-light source. The decomposition of RhB was carried out with 0.05 g of the catalyst dispersing uniformly into the RhB solution ($[\text{RhB}] = 10 \text{ ppm}$, 100 mL) in a Pyrex glass cell. Prior to the photocatalytic experiment, the suspensions were magnetically stirred in the dark for 45 min to ensure an

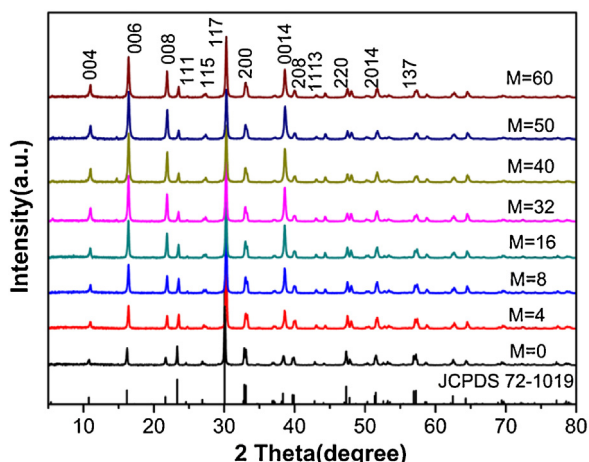


Fig. 1. XRD patterns of prepared BTO-M ($M=4, 8, 16, 32, 40, 50, 60$) samples with different mole ratio of salts to $\text{Bi}_4\text{Ti}_3\text{O}_{12}$ by MSS method and BTO-0 obtained by SSR method.

adsorption-desorption equilibrium. The samples were taken every 10 min including the sample powders and dyes. The dye solution was analyzed on a UV–vis spectrometer (UV-1800, Shimadzu) after the powders were removed by centrifuging. As a comparison, BTO-0 prepared by SSR method was also tested under visible-light irradiation.

3. Results and discussions

3.1. Structural analysis

Fig. 1 shows the XRD patterns of $\text{Bi}_4\text{Ti}_3\text{O}_{12}$ samples obtained by MSS and SSR methods. All the diffraction peaks can be indexed according to the standard data of orthorhombic $\text{Bi}_4\text{Ti}_3\text{O}_{12}$ with the space group Aba2 (JCPDS 72-1019). The sharp Bragg peaks shown in Fig. 1 indicate that well-crystallized orthorhombic $\text{Bi}_4\text{Ti}_3\text{O}_{12}$ are obtained by these two methods.

3.2. Morphological characterization

Scanning electron microscopy (SEM) was used to characterize the morphology and uniformity of the prepared samples (Fig. 2). As shown in Fig. 2a, the BTO-0 sample obtained by the SSR method shows irregular shapes with the particle size of 0.1–3 μm . However, in contrast to the BTO-0 sample, fairly uniform plate-like nanostructures of BTO-M are obtained through the MSS method as shown in Fig. 2b–h. By altering the amount of added salts, the shapes of the BTO-M samples change from fragmentary rectangular nanosheets with irregular periphery to inerratic rectangular nanosheets. The side length distribution of BTO-M is shown in Fig. 3. The average side length of the as prepared BTO-M nanosheets ranges from 2.4 to 1.8, 1.4, 1.0, 0.8, and 0.5 μm when changing the value of M from 4 to 8, 16, 32, 40, and 50. However, compared with BTO-50, the side length of BTO-60 is barely changed. Clearly, the addition amount of molten salts plays an important role in controlling the size of the resulting bismuth titanate. The insets in Fig. 2 show the magnified images of the side surfaces of the corresponding BTO-M samples. The average thickness of BTO-M nanosheets decreases (from 150 nm to 75–90 nm) as the M increases from 4 to 16. However, further increase of M value (BTO-M, $M=32, 40, 50, 60$) leads to limited decrease of thickness (ca. 55 nm). The results demonstrate that simultaneous control of the side length and thickness of BTO materials can be easily achieved via a facile MSS process by varying the added amount of the binary molten salts (NaCl and KCl).

The growth of $\text{Bi}_4\text{Ti}_3\text{O}_{12}$ in molten salts was anticipated to undergo an unconstrained dissolution-precipitation (or Oswald ripening) process. A long mass transport distance between $\text{Bi}_4\text{Ti}_3\text{O}_{12}$ particles due to the high M values might lower the growth rate of $\text{Bi}_4\text{Ti}_3\text{O}_{12}$, leading to the size reduction of the resulting BTO-M nanosheets [40]. The decreased particle size may substantially improve photocatalytic activities of BTO-M nanosheets by affecting the dynamics of photoinduced electrons and holes and thus their recombination process [41].

Transmission electron microscope (TEM) and high-resolution transmission electron microscope (HRTEM) were used to provide further insight into the microstructure of the products. The representative TEM images of the BTO-50 sample are shown in Fig. 4a. Well-defined nanosheets are visualized, exhibiting a rectangular outline with a side length of about 500 nm, in agreement with the SEM results (Fig. 2). Fig. 4b shows the representative HRTEM images of BTO-50 nanosheets. The lattice spacings of the two sets of lattices as marked are 2.70 Å and 2.72 Å, corresponding to (020) and (200) atomic planes of $\text{Bi}_4\text{Ti}_3\text{O}_{12}$, respectively [42]. Furthermore, the angle labeled in the corresponding fast-Fourier transform (FFT) pattern (inset in Fig. 4b) is 90°, which is identical to the theoretical value obtains for the angle between the (020) and (002) planes. The corresponding selected area electron diffraction (SAED) pattern shown in Fig. 4c indicates the single crystalline nature of the nanosheets. Based on the results described above, in-plane surfaces of BTO-50 nanosheets lie on (001) facets as shown in Fig. 4d.

3.3. UV–visible diffuse reflectance spectra

Fig. 5 shows the UV–vis diffuse reflectance spectra of BTO-M samples. Their band gaps could be derived using the equation $\alpha h\nu = A(h\nu - E_g)^{n/2}$, where α , A , $h\nu$ and E_g signify the absorption coefficient, proportionality constant, photon energy and band gap energy, respectively [43]. BTO possesses an indirect optical transition, and $n=4$ it is adopted. The inset of Fig. 5 shows the plot of the $(\alpha h\nu)^{1/2}$ versus E_g . The energy of the band gap is calculated from the tangent line in the plot as is shown in the inset of Fig. 5. The bandgaps of BTO-M ($M=4, 8, 16, 32, 40, 50, 60$) samples are 2.942, 2.934, 2.927, 2.921, 2.906, 2.88 and 2.892 eV, respectively. According to the theoretical first-principle calculation, the conduction bands of the $\text{Bi}_4\text{Ti}_3\text{O}_{12}$ are mainly contributed by Ti 3d + Bi 6p orbitals, while O 2p + Bi 6p hybrid orbitals mainly contribute to the valence band [44]. As reported previously, Bi–O and Ti–O dangling bonds as well as oxygen vacancies are formed on the surface of the nanosheet as the size of samples decrease [45]. Moreover, the photoinduced electrons are easily captured by the unpaired state of Bi atoms to form a relatively stable dipole which could become the trap center of the excitons, thus leading to trap-induced red shift of the absorption band edge of nanocrystalline BTO samples. Based on the UV–vis spectral observation, the size of BTO-M controlled by varying the amount of salts via the MSS method affects the optical absorption in the visible-light region, and thereby influences the photocatalytic activities of the BTO-M samples.

3.4. Photocatalytic kinetics for rhodamine B (RhB) degradation

The photocatalytic kinetics of the as-prepared catalysts with different morphologies are evaluated using RhB as the probe molecule under visible-light irradiation ($\lambda > 420 \text{ nm}$). Fig. 6a shows the time profiles of C/C_0 , where C_0 is the initial concentration of RhB at adsorption equilibrium before irradiation, and C is the corresponding concentration after a specific reaction time. As shown in Fig. 6a, no obvious photodegradation occurs with RhB when it is exposed to visible-light in the absence of BTO samples, while the degradation is significantly enhanced in the presence of the catalysts. The photocatalytic kinetics of BTO-M ($M=4-50$) increases as the value

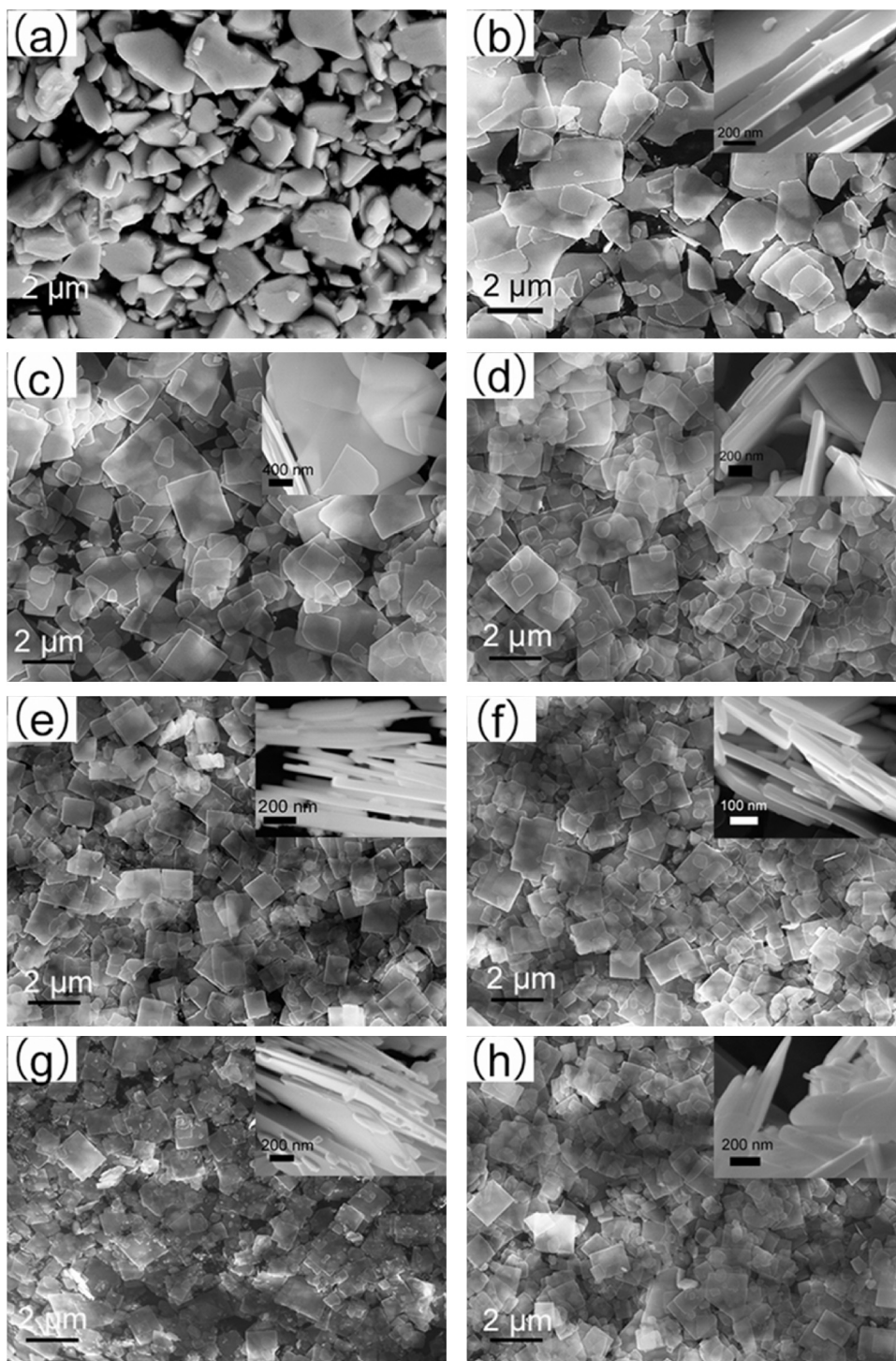


Fig. 2. SEM micrographs of BTO-*M* samples prepared by SSR (a) and MSS method at 800 °C: (b) BTO-4; (c) BTO-8; (d) BTO-16; (e) BTO-32; (f) BTO-40; (g) BTO-50; (h) BTO-60.

of *M* increases, and maximum is attained at *M*=50. With further increasing the value of *M* to 60, the corresponding photocatalytic kinetics is comparable to that of the BTO-50 sample. Furthermore, the photocatalytic degradation of RhB by BTO-0 obtained via SSR method is also compared. As shown in Fig. 6a, the rate of RhB degradation at BTO-0 is much slower compared with that at the samples prepared by the MSS method. Fig. 6b shows the linear relationship between $\ln(C_0/C)$ and time, indicating that the degradation of RhB follows pseudo-first-order kinetics. The apparent reaction rate constants (*k*) of BTO-*M* (*M*=0–60) for photodegradation of RhB are

displayed in Fig. 7. The sample BTO-50 shows the largest *k* value of 0.04671 min^{−1}, which is about 8.65 times of the *k* for the sample BTO-0. In other words, the MSS method shows a significant advantage over the SSR method in preparing BTO samples for the photodegradation of RhB.

Fig. 6c depicts the temporal absorption spectral changes of RhB in the presence of BTO-50. The absorption maximum of RhB at 553 nm drops rapidly, and ca. 93% of RhB is photodegraded after irradiation for 60 min. It is worth noting that the absorption maximum of the degraded solution exhibits hypsochromic shift along

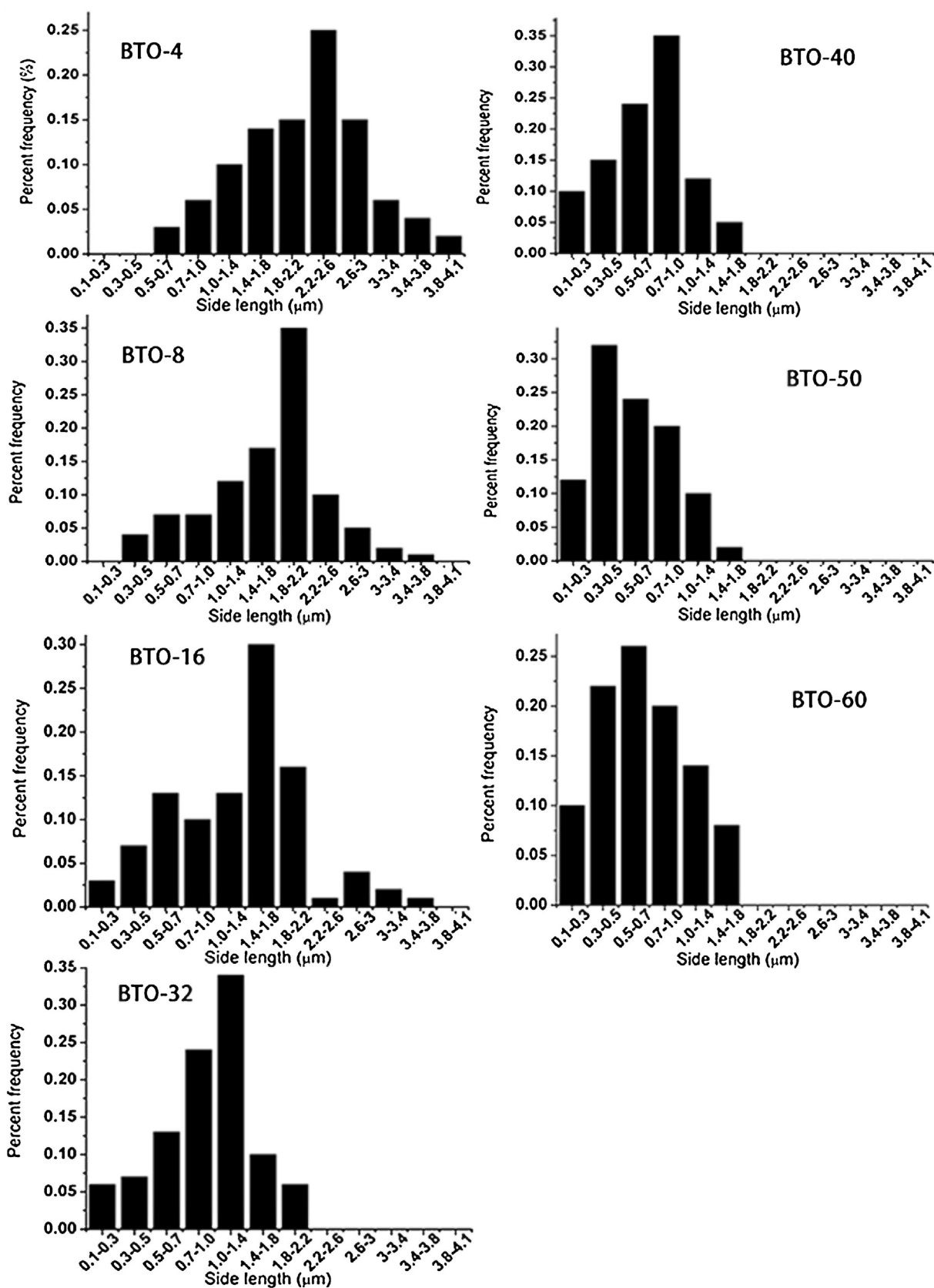


Fig. 3. Histograms of the side length distributions of BTO-M prepared via the MSS method.

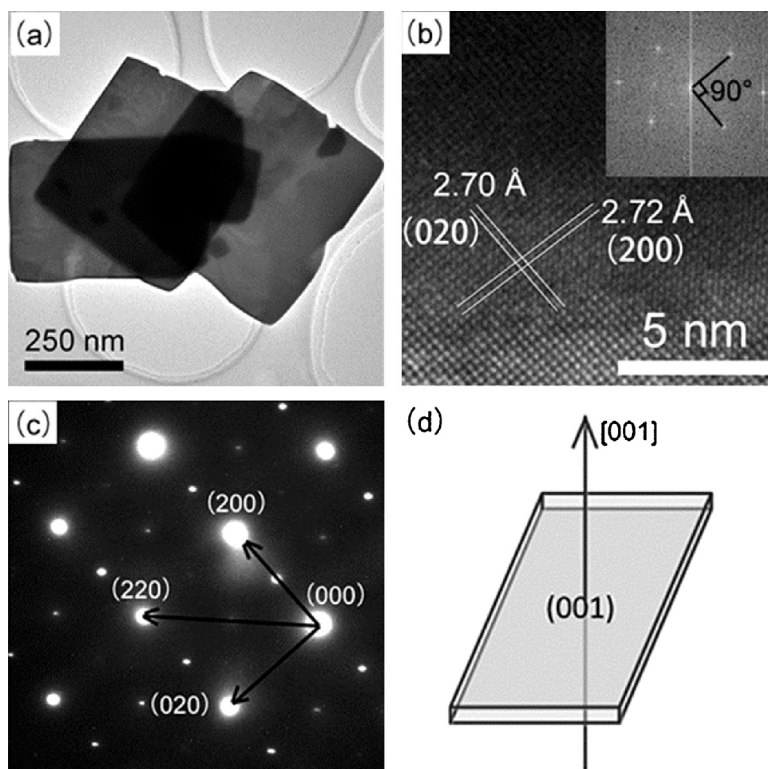


Fig. 4. (a) TEM, (b) HRTEM and (c) SAED images of BTO-50 nanosheets prepared by MSS method at 800 °C calcined for 2 h.

with the irradiation time. As reported earlier [46], this phenomenon may due to the formation and decomposition of a series of N-deethylated intermediates with the solution color changing from red to light green-yellow.

The photocatalytic kinetics of the semiconductors is a concert of many factors including surface area, crystallinity, structure of the material and so on [26,47]. The specific surface area of the BTO samples has been measured, and the detailed results are shown in Table 1. It can be seen that the specific surface area of BTO-*M* increases with the increasing of *M*, and reaches the maximum of 6.467 m² g⁻¹ at *M* = 50, in agreement with the SEM observation.

The apparent reaction rate constants normalized by surface area (*k'*) are also shown in Fig. 7. The increase of *k'* value is

significantly slower than that of *k*, suggesting that the specific surface area greatly affects the photocatalytic properties of the BTO-*M* samples. A larger surface area can provide more available surface active sites for the reaction [48], and also the increase in the specific surface area should improve the quantum efficiency of interfacial charge transfer [49]. Seen from Fig. 7, the values of *k'* of BTO-*M* (*M* = 4–60) are much higher than that of BTO-0, suggesting that the photocatalytic kinetics of BTO-*M* (*M* = 4–60) samples are also affected by other factors besides the specific surface area. It is worth noting that the *k'* of the samples increases with the value of *M* up to 16, above which, however, *k'* exhibits negligible dependence on *M*. This effect is consistent with the consequence of the thickness of the samples.

Single-crystal Bi₄Ti₃O₁₂ has strongly anisotropic ferroelectric properties due to its layered perovskite structure which consists of interleaved fluorite-like (Bi₂O₂)²⁺ layers and TiO₆ octahedra (perovskite slab) along the *c* axis, as is schematically illustrated in Fig. 8a. BTO single crystals exhibit spontaneous polarization (*P*_s) of 4 μC cm⁻² along the *c*-axis [24,39]. When the bulk of the ferroelectricity is broken by an interface, such as at the surface, a depolarization field will form. In order to form an energetically stable state, internal screening in the format of a space-charge region will form in the close proximity to the surface. The surface where a positive potential is produced by the polarization is termed C⁺ face, and the surface where a negative potential is produced by the polarization is named C⁻ face. Correspondingly, the internal electric fields will be established between C⁺ and C⁻ faces produced by polarization. The effect of the polarization in ferroelectric materials has been proven to be responsible for good photocatalytic activities [50]. When the BTO-*M* nanosheet exposed with {001} facets are irradiated by visible-light, photoinduced electron-hole pairs are formed and then driven apart by the internal electric fields between C⁺ and C⁻ surfaces (Fig. 8b) [51]. Therefore, the separation of photogenerated electron-hole pairs along [001] direction of BTO-*M* nanosheet will be promoted (Fig. 8c), the separation of

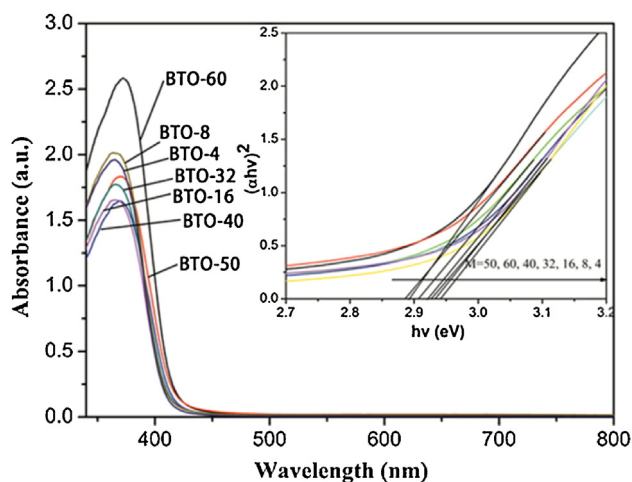


Fig. 5. UV-vis diffuse reflectance spectra of different BTO-*M* samples prepared by the MSS method (*M* = 4, 8, 16, 32, 40, 50, 60). Inset shows the band energy gaps of the corresponding BTO-*M* samples.

Table 1The BET surface area of BTO-*M* (*M* = 0, 4, 8, 16, 32, 40, 50, 60) samples.

Catalyst	BTO-0	BTO-4	BTO-8	BTO-16	BTO-32	BTO-40	BTO-50	BTO-60
BET surface area (m ² g ⁻¹)	1.425	2.303	3.129	3.582	5.12	6.023	6.467	6.277

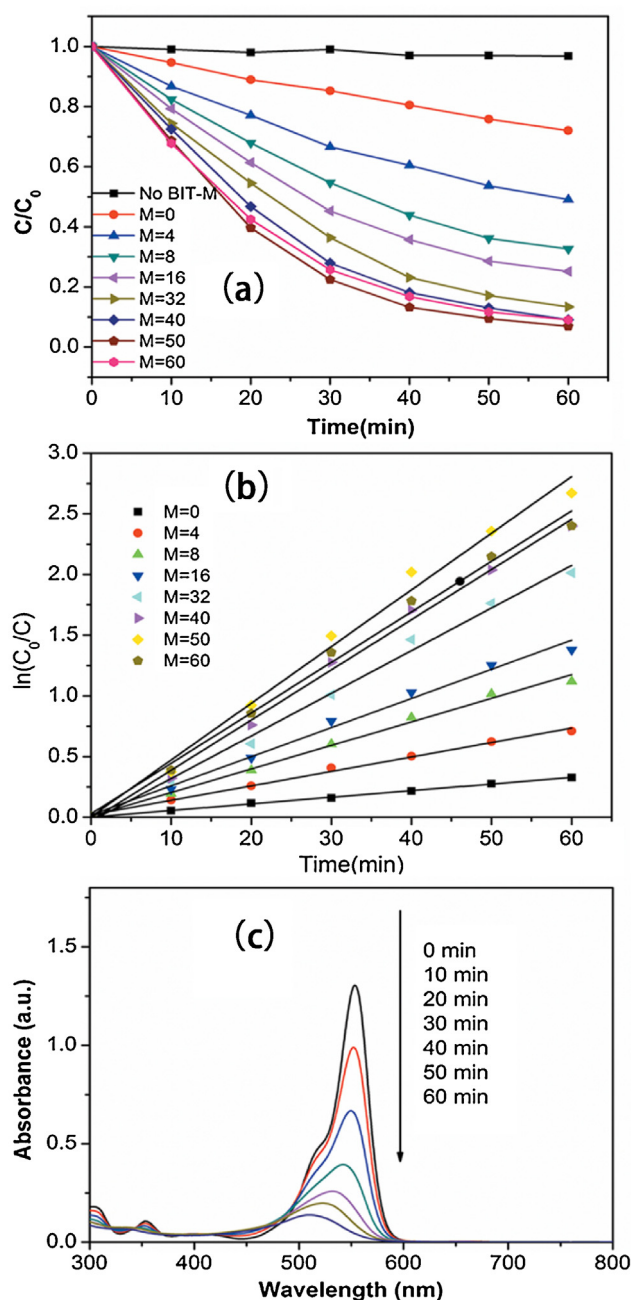


Fig. 6. (a) Degradation kinetics of RhB at the BTO samples under visible-light at pH = 5.3. (b) Linear simulation curves of RhB photodegradation. (c) Temporal absorption spectral changes of RhB in the presence of BTO-50 sample under visible-light irradiation. [RhB] = 10 ppm, [BTO] = 0.5 g/L. (For interpretation of the references to color in the text, the reader is referred to the web version of the article.)

carriers by the depolarisation fields also suppresses recombination rates thereby increasing carrier lifetimes, resulting in the observed higher photocatalytic kinetics for the BTO-*M* samples prepared by the MSS method than that by the SSR method. The benefits of internal electric fields have also been observed in the photodegradation of dyes via BiOCl single-crystalline nanosheets [19]. Based

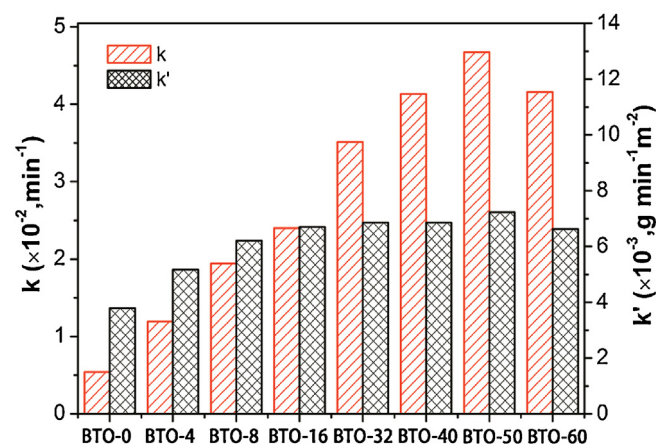


Fig. 7. Comparison of the apparent reaction rate constants for photodegradation of RhB using BTO-*M* samples under visible-light ($\lambda > 420$ nm) irradiation.

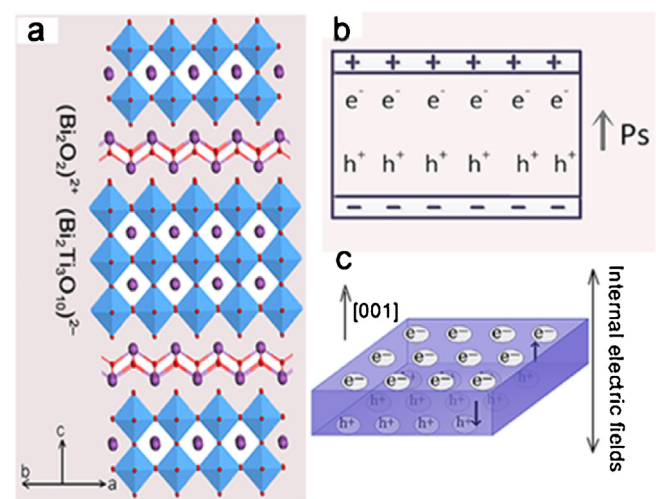


Fig. 8. (a) Schematic crystal structure of $\text{Bi}_4\text{Ti}_3\text{O}_{12}$ viewed along [110] direction. Aurivillius phase structure composed of interleaved $(\text{Bi}_2\text{O}_2)^{2+}$ layers and $(\text{Bi}_2\text{Ti}_3\text{O}_{10})^{2-}$ layers (blue, Ti; purple, Bi; red, O). (b) Proposed transfer mechanism of the photogenerated electron-hole pairs facilitated by Ps . (c) Model showing the direction of the internal electric field in BTO-*M* samples. (For interpretation of the references to color in this figure legend, the reader is referred to the web version of the article.)

on the above analyses, the gradual decrease in thickness of BTO-*M* (*M* = 4–16) samples is beneficial to the photocatalytic kinetics by reducing the charge transfer distance. Consequently, the value of k' increases with decreasing the thickness of BTO-*M* (*M* = 4–16), and nearly levels off for BTO-*M* (*M* = 16–60). Therefore, the large BET surface derived from the small particle size and the thickness of BTO-*M* (*M* = 4–60) contribute to the subsequent enhancement in photocatalytic kinetics of the samples.

In order to verify the charge separation effect under the internal electric field, the local surface potentials of BTO sample in dark and with light irradiation were measured with Kelvin probe force microscopy (KPFM) method. Due to the absence of inversion center of crystal structure there exists an intrinsic built-in electric field in BTO as a consequence of spontaneous polarization. When

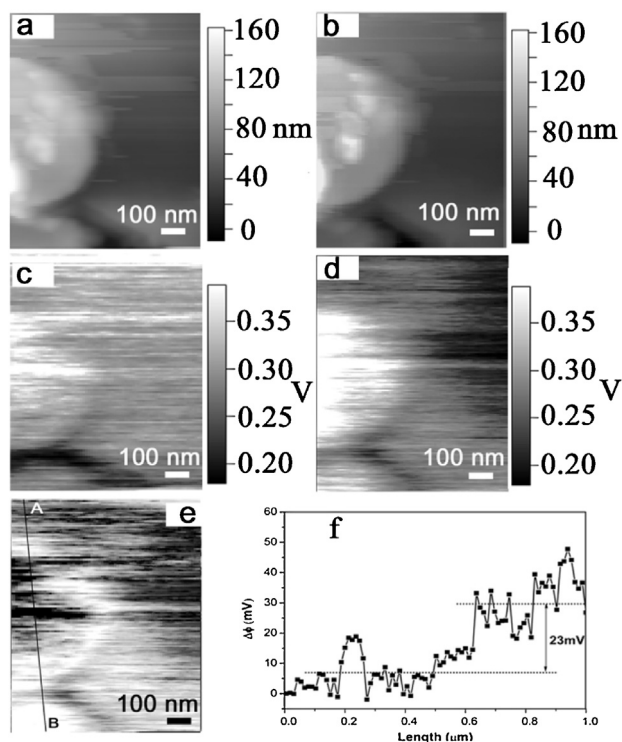


Fig. 9. The topography and surface potential profiles of BTO-50 nanosheet measured on glass slide surface with and without visible-light irradiation. The KPFM topographies of BTO-50 in dark and under visible-light irradiation are shown in (a) and (b), respectively. (c) The corresponding surface potential mapping of BTO-50 measured in dark and, (d) the potential mapping under visible-light irradiation. (e) The differential map by subtracting image (d) from image (c). (f) Cross-sections obtained along the lines A–B in image (e).

irradiating the BTO sample with visible-light, the photoinduced electrons and holes can be effectively separated under the internal electric field. The charge separation process consequently leads to a change of surface potential of both surfaces with different signs [52], which can be illustrated from KPFM results.

Fig. 9a and b shows the topography mapping of BTO-50 sample in dark and during visible-light irradiation, respectively. Apparently, no surface structure change is induced by the light irradiation in topographic measurements of the sample. However, noticeable difference in the surface potential can be clearly observed between the image measured in dark (Fig. 9c) and the one measured during visible-light irradiation (Fig. 9d). Explicitly, during light irradiation, the surface potential of the sample is dramatically decreased. Indeed, beside the charge separation process, the electron-excitation process is also contributing to the change of surface potential since a filling of conduction band by excited electrons is involved. Because this effect has equal contributions to all surfaces of the sample, there would be no structural change of the surface potential image subtracting one image from the other. However, the structural change in the surface potential is clearly observed as shown in Fig. 9e obtained by subtracting Fig. 9d from Fig. 9c. This structural change is reflected by the light and dark fluctuation in Fig. 9e, which is owing to the charge separation driven by the internal electric fields. Fig. 9f shows the surface potential line profile along A–B in Fig. 9e. The average difference in the surface potential between different areas of the sample is estimated to be about 23 mV. The KPFM study clearly manifests that the BTO nanosheet exposed with {001} facets possesses internal electric fields produced by spontaneous polarization, which can facilitate the separation of photoinduced electrons and holes.

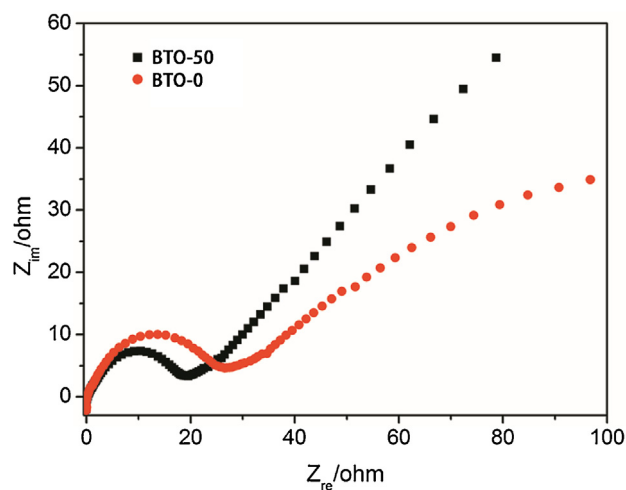


Fig. 10. EIS Nyquist plots (Z_{im} vs. Z_{re}) for the photoelectrodes of BTO-50 prepared by MSS method and BTO-0 prepared by SSR method in 5 mM $[\text{Fe}(\text{CN})_6]^{3-/4-}$ and 0.1 M KCl solution at pH = 7 under visible-light irradiation ($\lambda > 420$ nm).

In order to evaluate the electron-transfer capacity of BTO-50 and BTO-0, the electrochemical impedance spectroscopy was measured using a 0.1 M $[\text{Fe}(\text{CN})_6]^{3-/4-}$ solution as the electrical probe (Fig. 10). The diagrams of these two photoelectrodes include a semicircle part reflect the charge transfer process and a linear line with a slope of 45° belonged to the diffusion-controlled step [53]. The electron-transfer resistance (R_{ct}) can be evaluated by measuring its diameter. Under visible-light irradiation, R_{ct} of the BTO-50 electrode calculated to be ca. 17 Ω , less than the R_{ct} of the BTO-0 electrode (ca. 27 Ω), indicating that the BTO-50 nanosheet is more efficient for photoinduced charge separation and transfer in comparison to that of the BTO-0 sample. Therefore, the BTO- M samples prepared by the MSS method exhibit more efficient photodegradation of RhB for the nanosheet structure with exposed {001} facets which could facilitate the charge separation and transfer, however, the sample obtained by SSR method have irregular shapes which is not in favor of charge separate and transfer, indicating the superiority of the MSS method in comparison to the SSR method.

4. Conclusions

Size-controllable syntheses of $\text{Bi}_4\text{Ti}_3\text{O}_{12}$ nanosheet with exposed {001} facets has been achieved via a convenient molten salt process by varying the amounts of NaCl and KCl. The side length of the BTO- M ($M = 4-60$) samples gradually decreases as the amount of salts increases and reaches the minimum at $M = 50$. The BTO- M ($M = 4-60$) samples exhibit size-dependent photoactivity for degradation of RhB in visible-light region. Importantly, all the products obtained by the MSS method exhibit much higher photocatalytic kinetics than the BTO-0 prepared by the SSR method, indicating the advantage of the present method for preparing BTO photocatalyst. In particular, the BTO-50 with the smallest side length and thickness shows the highest photocatalytic kinetics, which is 8.65 times higher than that of BTO-0. The highly faceted surfaces, short charge transport distance to the surface and favorable internal electric fields due to photoinduced polarization are investigated to be crucial factors for the improved photocatalytic kinetics of BTO- M samples.

Acknowledgments

Financial support by the National Nature Science Foundation of China (Grant Nos. 21173261, 21001113), the "One Hundred Talents Project Foundation Program" of Chinese Academy of

Sciences, International Science & Technology Cooperation Program of Xinjiang Uygur Autonomous Region (20126017), the CAS/SAFEA International Partnership Program for Creative Research Teams, the Excellent Youth Foundation of Xinjiang Uygur Autonomous Region (2013711004), the “Cross-Cooperation Program for Creative Research Teams” of Chinese Academy of Sciences, the “Western Action Plan” (KGZD-EW-502) and the “Western Light Joint Scholar” program of Chinese Academy of Sciences (LHXZ201001) is gratefully acknowledged. TX also acknowledges the support from the U.S. National Science Foundation (CBET-1150617).

References

- [1] S. Dhar, W.L. Daniel, D.A. Giljohann, C.A. Mirkin, S.J. Lippard, *J. Am. Chem. Soc.* 131 (2009) 14652–14653.
- [2] S.-I. Naya, A. Inoue, H. Tada, *J. Am. Chem. Soc.* 132 (2010) 6292–6293.
- [3] A. Tanaka, K. Hashimoto, H. Kominami, *J. Am. Chem. Soc.* 134 (2012) 14526–14533.
- [4] X.T. Hong, Z.P. Wang, W.M. Cai, F. Lu, J. Zhang, Y.Z. Yang, N. Ma, Y.J. Liu, *Chem. Mater.* 17 (2005) 1548–1552.
- [5] A. Kasahara, K. Nukumizu, G. Hitoki, T. Takata, J.N. Kondo, M. Hara, H. Kobayashi, K. Domen, *J. Phys. Chem. A* 106 (2002) 6750–6753.
- [6] G. Hitoki, T. Takata, J.N. Kondo, M. Hara, H. Kobayashi, K. Domen, *Chem. Commun.* (16) (2002) 1698–1699.
- [7] A. Ishikawa, T. Takata, J.N. Kondo, M. Hara, H. Kobayashi, K. Domen, *J. Am. Chem. Soc.* 124 (2002) 13547–13553.
- [8] S.M. Ji, P.H. Borse, H.G. Kim, D.W. Hwang, J.S. Jang, S.W. Bae, J.S. Lee, *Phys. Chem. Chem. Phys.* 7 (2005) 1315–1321.
- [9] R. Asahi, T. Morikawa, T. Ohwaki, K. Aoki, Y. Taga, *Science* 293 (2001) 269–271.
- [10] Z.G. Zou, J.H. Ye, K. Sayama, H. Arakawa, *Nature* 414 (2001) 625–627.
- [11] H. Kato, A. Kudo, *J. Phys. Chem. B* 106 (2002) 5029–5034.
- [12] D.W. Hwang, H.G. Kim, J.S. Lee, J. Kim, W. Li, S.H. Oh, *J. Phys. Chem. B* 109 (2005) 2093–2102.
- [13] D. Wang, J. Ye, H. Kitazawa, T. Kimura, *J. Phys. Chem. C* 111 (2007) 12848–12854.
- [14] D.F. Wang, J.H. Ye, T. Kako, T. Kimura, *J. Phys. Chem. B* 110 (2006) 15824–15830.
- [15] M. Tian, W. Shangguan, J. Yuan, L. Jiang, M. Chen, J. Shi, Z. Ouyang, S. Wang, *Appl. Catal. A* 309 (2006) 76–84.
- [16] T. Ohno, K. Sarukawa, M. Matsumura, *New J. Chem.* 26 (2002) 1167–1170.
- [17] E. Bae, T. Ohno, *Appl. Catal. B* 91 (2009) 634–639.
- [18] N. Murakami, Y. Kurihara, T. Tsubota, T. Ohno, *J. Phys. Chem. C* 113 (2009) 3062–3069.
- [19] J. Jiang, K. Zhao, X. Xiao, L. Zhang, *J. Am. Chem. Soc.* 134 (2012) 4473–4476.
- [20] J. Zhu, S. Wang, Z. Bian, S. Xie, C. Cai, J. Wang, H. Yang, H. Li, *CrystEngComm* 12 (2010) 2219–2224.
- [21] X.H. Yang, Z. Li, G. Liu, J. Xing, C. Sun, H.G. Yang, C. Li, *CrystEngComm* 13 (2011) 1378–1383.
- [22] M. Vehkamaeki, T. Hatanpaa, M. Kemell, M. Ritala, M. Leskelae, *Chem. Mater.* 18 (2006) 3883–3888.
- [23] D.J. Singh, S.S.A. Seo, H.N. Lee, *Phys. Rev. B* 82 (2010) 180103.
- [24] S.E. Cummins, L.E. Cross, *J. Appl. Phys.* 39 (1968) 2268.
- [25] H. Zhang, G. Chen, X. Li, *Solid State Ionics* 180 (2009) 1599–1603.
- [26] W.F. Yao, X.H. Xu, H. Wang, J.T. Zhou, X.N. Yang, Y. Zhang, S.X. Shang, B.B. Huang, *J. Appl. Phys.* 52 (2004) 109–116.
- [27] X. Lin, Q.F. Guan, H.B. Li, H.J. Li, C.H. Ba, H.D. Deng, *Acta Phys. Chim. Sin.* 28 (2012) 1481–1488.
- [28] X. Lin, P. Lu, Q.F. Guan, H.B. Li, H.J. Li, J. Cai, Y. Zou, *Acta Phys. Chim. Sin.* 28 (2012) 1978–1984.
- [29] D. Hou, W. Luo, Y. Huang, J.C. Yu, X. Hu, *Nanoscale* 5 (2013) 2028–2035.
- [30] Y. Mao, S. Banerjee, S.S. Wong, *J. Am. Chem. Soc.* 125 (2003) 15718–15719.
- [31] B. Liu, H.M. Chen, C. Liu, S.C. Andrews, C. Hahn, P. Yang, *J. Am. Chem. Soc.* 135 (2013) 9995–9998.
- [32] A. Sen, U.N. Maiti, S. Maiti, K.K. Chattopadhyay, *J. Mater. Sci.* 48 (2013) 3967–3974.
- [33] H. Hao, H.X. Liu, Y. Liu, M.H. Cao, S.X. Ouyang, *J. Am. Ceram. Soc.* 90 (2007) 1659–1662.
- [34] C.Y. Xu, L. Zhen, R. Yang, Z.L. Wang, *J. Am. Chem. Soc.* 129 (2007) 15444–15445.
- [35] B. Brahmaraout, G.L. Messing, S. Trolier-McKinstry, *J. Am. Ceram. Soc.* 82 (1999) 1565–1568.
- [36] J.X. Sun, G. Chen, J. Pei, R.C. Jin, Q. Wang, X.Y. Guang, *J. Mater. Chem.* 22 (2012) 5609–5614.
- [37] Y.X. Li, L. Zang, Y. Li, Y. Liu, C.Y. Liu, Y. Zhang, H.Q. He, C.Y. Wang, *Chem. Mater.* 25 (2013) 2045–2050.
- [38] R.H. Arendt, *J. Solid State Chem.* 8 (1973) 339–347.
- [39] Y. Kitanaka, S. Katayama, Y. Noguchi, M. Miyayama, *Jpn. J. Appl. Phys.* 46 (2007) 7028–7030.
- [40] Y.M. Kan, X.H. Jin, P.L. Wang, Y.X. Li, Y.B. Cheng, D.S. Yan, *Mater. Res. Bull.* 38 (2003) 567–576.
- [41] X. Chen, S. Shen, L. Guo, S.S. Mao, *Chem. Rev.* 110 (2010) 6503–6570.
- [42] J.F. Dorrian, R.E. Newnham, M.I. Kay, D.K. Smith, *Ferroelectrics* 3 (1971) 17–27.
- [43] J.W. Tang, Z.G. Zou, J.H. Ye, *J. Phys. Chem. B* 107 (2003) 14265–14269.
- [44] W. Wei, Y. Dai, B. Huang, *J. Phys. Chem. C* 113 (2009) 5658–5663.
- [45] F. Wang, J. Wang, X. Zhong, B. Li, J. Liu, D. Wu, D. Mo, D. Guo, S. Yuan, K. Zhang, Y. Zhou, *CrystEngComm* 15 (2013) 1397–1403.
- [46] C.C. Chen, W. Zhao, P.X. Lei, J.C. Zhao, N. Serponer, *Chem. Eur. J.* 10 (2004) 1956–1965.
- [47] G. Liu, L. Wang, H.G. Yang, H.M. Cheng, G.Q. Lu, *J. Mater. Chem.* 20 (2010) 831–843.
- [48] M.R. Hoffmann, S.T. Martin, W. Choi, D.W. Bahnemann, *Chem. Rev.* 95 (1995) 69–96.
- [49] W.G. Becker, M.M. Truong, C.C. Ai, N.N. Hamel, *J. Phys. Chem.* 93 (1989) 4882–4886.
- [50] E. Gutmann, A. Benke, K. Gerth, H. Böttcher, E. Mehner, C. Klein, U. Krause-Buchholz, U. Bergmann, W. Pompe, D.C. Meyer, *J. Phys. Chem. C* 116 (2012) 5383–5393.
- [51] Y. Sun, B.S. Eller, R.J. Nemanich, *J. Appl. Phys.* 110 (2011) 084303.
- [52] W. Melitz, J. Shen, A.C. Kummel, S. Lee, *Surf. Sci. Rep.* 66 (2011) 1–27.
- [53] R.J. Pei, Z.L. Cheng, E.K. Wang, X.R. Yang, *Biosens. Bioelectron.* 16 (2001) 355–361.